Original citation:
Girão Coelho, Ana M. and Mottram, J. Toby. (2017) Numerical evaluation of pin-bearing strength for the design of bolted connections of pultruded FRP material. Journal of Composites for Construction, 21 (5).

Permanent WRAP URL:
http://wrap.warwick.ac.uk/85091

Publisher's statement:
Published version: https://doi.org/10.1061/(ASCE)CC.1943-5614.0000809

Numerical Evaluation of Pin-Bearing Strength for the Design of Bolted Connections of Pultruded FRP material

Ana M. Girão Coelho
Lecturer (former Marie Curie IEF Research Fellow at the University of Warwick)
(ana.girao-coelho@ncl.ac.uk)
School of Engineering and Geosciences, Newcastle University, Newcastle upon Tyne, UK

J. Toby Mottram
Professor
(corresponding author: j.t.mottram@warwick.ac.uk)
School of Engineering, University of Warwick, Coventry, UK
orcid.org/0000-0002-2750-8125

Abstract: Presented in this paper are finite element (Abaqus) predictions for the strength of a pultruded fibre reinforced polymer material subjected to pin-bearing loading with hole clearance. One of the distinct modes of failure in steel bolted connections is bearing. It is caused by the compression action from the shaft pressing into the laminate, and when there is no lateral restraint the mechanism observed at maximum load shows 'brooming' for delamination failure.

Each lamina in the glass fibre polyester matrix material is modelled as a homogeneous, anisotropic continuum and a relative very thin resin layer is assumed to contain any delamination cracking between stacked layers. A cohesive zone model is implemented to predict the size and location of the initial delamination, as well as the load-carrying capacity in a pin-bearing specimen. Finite element simulations (as virtual tests) are performed at the mesoscale level to validate the modelling methodology against experimental strength test results with delamination failure, and to show how pin-bearing strength varies with parameter changes. For an example of the knowledge to be gained for the design of bolted connections, the parameteric study where the mat reinforcement is either continuous strand or triaxial (+45º/90º/-45º/chopped strand) shows the latter does not provide an increase in pin-bearing strength.

Author keywords: Damage mechanics; Bearing failure; Finite element modelling; Pultruded material.

Introduction

Shapes made by the pultrusion composite processing method consist of thin-walled laminated panels of glass Fibre Reinforced Polymer (FRP) matrix connected to form open or closed cross-sections. Because I, wide flange, channel, box and leg-angle shapes mimic steel sections it is natural that frame construction follows what is seen in conventional steelwork (Creative Pultrusions 2016; Strongwell 2016; Turvey 2000). Being lightweight and resistant to corrosion, and having expected low life cycle costing, pultruded structures are increasingly used where these attributes meet the requirements of the construction project, such as for pedestrian bridges (Anonymous 2016).

Introduced in Mottram and Zafari (2011) is the rationale for steel bolting to be a main method of connection (Creative Pultrusions 2016; Strongwell 2016), and the requirement that, for strength design, a reliable test method is needed to determine bearing strengths. The *bearing strength* is an important material parameter for static strength design (Bank 2006; Mottram and Turvey 2003), and can be characterized as the resistance of the material to a fastener loaded hole. Strength depends on a number of parameters including: FRP thickness (t); FRP mechanical properties; FRP material orientation to the bearing force; bolt material; bolt diameter (d); clearance hole size. In bolted lap-joints the end distance (e_1), which is the distance from the centre of the hole to the free edge perpendicular to the loading direction has to exceed a limiting value for the bearing failure mode to govern.

An advantage for bolted connection design failing in the bearing mode is that it might provide the connection/joint with a degree of damage tolerance and structural integrity. Bearing failure can be enhanced by: (i) correctly sizing the connection, usually end distance to fastener diameter ratio $e_1/d \geq 3$ providing the width to fastener ratio is 4 or higher, see Bank (2006), and Girão Coelho and Mottram (2015a); (ii) the choice of the fibre reinforcements in the lamination stacking sequence.

Mottram and Zafari (2011) justify why the measurement of bearing strength for design calculations must be for the lower bound pin-bearing value. The pin-bearing condition assumes the steel bolt shaft has no thread in bearing and that there is no lateral restraint, which will not initially exist in practice because the washer, nut, bolt combination should be tightened. The paper explains the reasons for having a strength test method for pin-bearing strength with a plate-shaped coupon that is no larger in size than, say 80×80×*t* mm. Using an in-house test approach, detailed in Mottram and Zafari (2011) or Matharu (2014), numerous test results have been reported from programmes of characterization work (see also Zafari and Mottram 2012) to understand the variations in pin-bearing strength and characteristic values for pultruded materials. Two different materials were studied, and in the test matrix parameters were: four bolt diameters, e.g. 9.53 mm (3/8 in.), 12.7 mm (1/2 in.), 15.8 (5/8 in.) and 25.4 mm (1 in.) (Mottram and Zafari 2011) or M10, M12, M16 and M20 (Matharu 2014); different material orientations (e.g. 0^{o}, 90^{o} and 45^{o}); non-aged and hot-wet aged materials. One aim of the characterization work was to obtain data on how pin-bearing strengths might change in the field due to the long-term effect of exposure to a site's environment.

Both materials were from the American pultruder Creative Pultrusions (2016) having glass fibre reinforcement in the form of alternative layers of unidirectional rovings and a mat, and a fire-retardant matrix of an isophthalic polyester polymer. For the Mottram Zafari (2011) and Zafari and Mottram (2012) tests the pultruded material was from the standard 1525 series having mat reinforcement of a Continuous Strand Mat (CSM) having a random arrangement of continuous fibres. Matharu's (2014) work was with material from the Pultex® SuperStructural 1525 series, and the main difference is that the mat reinforcement is triaxial, having unidirectional fibres at 90^{o}, and $\pm 45^{o}$ and a 'thick' backing of a chopped strand fibres. Another difference in the test matrix with Matharu is that testing was with and without bolt thread in bearing; only the latter connection condition can be linked to the Finite Element (FE) work presented in this paper.

The FE modelling methodology applied by the authors uses options solely available from the general purpose software Abaqus with its implicit solver (2016). Girão Coelho *et al*. (2016) introduce, and show how the approach is modelling the various failure modes, and, in particular, for the parametric studies given later the critical mode of progressive delamination using cohesive zone models. A similar approach using Abaqus/Explicit has been reported by Du *et al*. (2016) with their progressive damage analysis implemented via a user subroutine VUMAT. Because no customized user-subroutines are required with the author's modelling methodology the computational results using Abaqus implicit can be universally reproduced. Simulation outputs for pin-bearing strengths will be validated using non-aged test results from Matharu (2014), and in a strength comparison using data from Mottram and Zafari (2011) for changing the mat reinforcement. The main contribution of this paper is the predictions from a series of parametric studies to investigate how pin-bearing strength might vary with changes in the fibre reinforcement.

Fundamental Behaviour and Analysis Approach

Bearing failure is a mode showing local crushing and delamination of the laminated material in direct contact with the steel bolt shaft (Bank 2006; Mottram and Turvey 2003). The bearing strength of monolithic materials (e.g. steel) is generally evaluated without lateral restraint or through thickness constraint from a bolt tightening. Application of this test condition with FRP composites allows delamination fracturing to occur. In this paper the word *delamination* has the meaning for the formation and growth of a flat flaw in an initially flawless interface (between two previously 'bonded' laminae) that grows into a sizeable delamination crack. With PFRP materials this failure mechanism leads to the lowest bearing strength.

The presence of composite material viscoelasticity (Mottram 2005), and the influence of structural actions on the bolted connection ensure that it will be unreliable to assume there can always be lateral restraint at the end of the design working life, which can for a structure be, 50 or 100 years. It is for this reason (Mottram and Zafari 2011) that the *pin-bearing strength* has to be the strength used in design calculations for bolted connection strength design.

The FE study presented next to model the bearing behaviour includes a *continuum damage model* with a *cohesive zone approach*. Continuum damage models address the *intralaminar failure mechanisms* from a global standpoint, whereas if the analyst used individual damage mechanisms they would be homogenized and constructed around a failure criterion (Knops 2008). This approach is the least complex and uses the composite lay-up modeller tool within the Abaqus (2016) pre-processor to define the individual laminae through a laminate thickness. Each layer is cohesively bonded together to form the *lamination with interfaces* assumed to have a thickness of $10^{-3}t_{\mathrm{lay}}$, where t_{lay} is the thickness of the thinnest layer either side of the interface. Values for t_{lay} are introduced in the section for the *Description of the Model*. This modelling dimension plays the role of a length scale, and it has been shown by Girão Coelho (2016) that the thickness of the cohesive interface does not affect the computational performance provided its thickness is small enough compared to t_{lay}.

Modelling of Progressive Delamination Using Cohesive Zone Models

Delamination failure is the separation of reinforcing layers from each other, as a consequence of shear stresses acting in planes parallel to the layers' interfaces and/or tensile stresses acting in the through-thickness direction. This phenomenon is a typical *crack growth* problem and is treated in the framework of fracture mechanics (Girão Coelho 2016). Today, the most popular computational method for the prediction of delamination failure is based on *cohesive zone models* that provide a natural bridge between strength-based models and energy-based models for fracture. This allows delamination to be described by a single framework that covers a range of applications for which, on their own, neither a strength nor an energy criterion might not be sufficient.

Cohesive zone models consider fracture as a gradual phenomenon in which separation takes place across an extended crack tip, or cohesive zone, and is resisted by cohesive tractions (Ortiz and

Pandolfi 1999). Thus cohesive zone elements do not represent any physical material, but describe the cohesive forces which occur when layers in the lamination are being pulled apart. In FE modelling, cohesive zone elements are placed between the continuum elements used to model the individual laminae. A key analysis feature of these elements is that they include the effect of first delamination failure, and the subsequent crack propagation by means of critical strain energy release rates.

In our modelling methodology, see Girão Coelho *et al*. (2016), the simulation of interlaminar damage is based on the cohesive zone approach using the Abaqus three-dimensional cohesive element COH3D8. The study is performed in the quasi-static regime. The traction-separation law formulation assumes a non-zero elastic stiffness of the cohesive zone, which is physically motivated by the reduced stiffness of the matrix-rich very thin interface layer (t_{lay}) as compared to a perfect bond assumed to exist between the fibres and the surrounding polymer matrix. From a numerical point of view, this elastic stiffness can be understood as a penalty-type enforcement of displacement continuity in the elastic range.

A quadratic stress criterion is used for the *damage initiation criterion*. To specify the conditions for separation in the cohesive zone model the following expression is chosen (Brewer and Lagace 1988; Camanho *et al*. 2003):

$$\left(\frac{\langle\sigma_{\mathrm{n}}\rangle}{f_{\mathrm{I}}}\right)^2+\left(\frac{\sigma_{\mathrm{s}}}{f_{\mathrm{II}}}\right)^2+\left(\frac{\sigma_{\mathrm{t}}}{f_{\mathrm{III}}}\right)^2=1 \tag{1}$$

where σ_{n} is the stress in pure opening mode, σ_{s} is the stress in the first shear direction, σ_{t} is the stress in the second shear direction, f_{I} (opening), f_{II} (sliding)) and f_{III} (tearing) are the peak strength values in the same directions, and:

$$\langle\sigma_{\mathrm{n}}\rangle=\sigma_{\mathrm{n}} \quad \text{for} \quad \sigma_{\mathrm{n}}>0 \qquad \text{and} \qquad \langle\sigma_{\mathrm{n}}\rangle=0 \quad \text{for} \quad \sigma_{\mathrm{n}}\leq 0\,. \tag{2}$$

The latter modelling constraint in Eq. (2) is because compressive normal stresses cannot open a delamination crack.

Progression of damage at the interfaces is modelled using a linear softening law and a critical mixed mode energy behavior based on the Benzeggagh-Kenane criterion (1996), which is described by the following expression:

$$G_{\mathrm{c}} = G_{\mathrm{I,c}} + \left(G_{\mathrm{II,c}} - G_{\mathrm{I,c}}\right)\left[G_{\mathrm{II}} / \left(G_{\mathrm{I}} + G_{\mathrm{II}}\right)\right]^{\eta}. \tag{3}$$

In Eq. (3) $G_{\mathrm{m,c}}$ (with m = I, II, III) is for the total critical strain energy release rate associated with delamination mode m, and η is for the semi-empirical criterion exponent applied to delamination initiation and growth. Based on the argument given by Girão Coelho (2016) exponent η is assumed to be 1.5. Illustrated in Figs. 1(a) to 1(c) are the three distinct opening modes that can occur singularly or interact together to cause the initiation and formation of a delamination failure.

The use of cohesive zone models requires that a very fine mesh specification is used to ensure that sufficient interface elements exist within the cohesive zone length where the crack tip is moving. If the mesh design happens to be too coarse, the cohesive stress at the discontinuity may not even reach the interfacial strength and, as a result, the required failure mode is missed. Falk *et al*. (2001) suggest a minimum of two to five elements in this cohesive zone length in order to perform a reliable simulation. Turon *et al*. (2000) indicate that for typical graphite-epoxy or glass-epoxy FRP materials, the length of the cohesive zone should be smaller than one or two millimetres. As a consequence, the mesh size required in order to have more than two elements in the cohesive zone should be smaller than half a millimetre. For full-sized structural models of pultruded shapes and structures this has the obvious consequence of a computationally expensive solution. Current numerical simulations for the 80×80×9.5 mm pin-bearing specimen comply with the cohesive zone element mesh size requirements specified by the first author (Girão Coelho 2016) to allow stable numerical simulations of interface delamination.

Finite Element Validation of Strength Behaviour

A general FE model for the pin-bearing problem is developed and validated in this section using experimental strength results from the PhD work by Matharu (2014). Note that the objective of the FE work is to obtained predictions for the pin-bearing strength, which is established by the maximum test load (or stress, which is this load divided by the projected bearing area given by pin diameter times specimen thickness). There are engineering/scientific reasons why the FE simulations might not be numerically reliable in predicting the onset of damage and all of the modes of failure that occur prior to peak load. There is a likelihood that piror to loading there are already matrix cracks (running parallel to the unidirectional fibre) because of residual thermal strain owing to the cooling down from a temperature of 150^{o}C in the pultrusion composite processing.What is known from the extensive programme of static strength tests by Matharu (2014), and by Mottram and Zafari (2011), is that when the bearing load is aligned in the direction of pultrusion the load-stroke curve (testing machine displacement) is virtually linear elastic until to ultimate failure, which always occurs with a noticeable load reduction and audible acoustic emissions. This signal of ultimate failure is too pronounced to be for initial/new matrix cracking, and when the post-failure load is released inspection of the bearing surface shows there to be interfacial delamination fractures. This is the authors' evidence-based justification for how the FE invetigation was carried out and reported in this paper.

Matharu (2014) tests are for pultruded material taken from the web of a Pultrex® SuperStructural wide flange shape with nominal thickness of 9.53 mm (3/8 in.) (Creative Pultrusions 2016); the measured thickness is closer to 9.6 mm. The test matrix has plain steel pins of four metric diameters from 10 to 20 mm diameter with a clearance hole size that introduced the maximum allowable fabrication tolerance using the guidance in Anonymous (2012) from the Pultrusion Industry Council, USA. The technical reason for the maximum is that the bigger the hole clearance is, the lower is the pin-bearing strength (Yuan 1996), and for a safe design the lowest characteristic strength is required (Mottram and Zafari 2011). Without the fabrication tolerance the recommended clearance size is 1.6 mm (or 1/16 in.) (Anonymous 2012; Creative Pultrusions 2106;

Strongwell 2012). The nominal clearance ($d_0 - d$) is 2.2 mm (given by 1.6 mm clearance +0.4 mm tolerance) for M10 and 2.4 mm (1.6 mm clearance +0.8 mm tolerance) for M12, M16 and M20 bolt sizes. After drilling a pilot hole of diameter less than required the final hole dimeter to ±0.02 mm was prepared using a Cinccinati Arrow 450 Milling machine. Batches of ten nominally identical specimens were tested to determine the pin-bearing strength that is statistically analysed and critically evaluated by Matharu (2014).

The geometry was taken comparable to the experimental set-up, with the pin diameter as FE modelling parameter. Fig. 2 defines the specimen geometry and shows the layered structure of the SuperStructural web material.

Specific characteristics and attributes that were incorporated into the modelling are:

1. Based on the relatively high stiffness of the steel pin with respect to the longitudinal web material, *c.f.* 210 kN/mm^2 (BS EN 1993-1-1:2005) to 21.3 kN/mm^2 (Creative Pultrusions 2016)), the bearing load is exerted by a rigid (circular smooth) pin, this is shown in Fig. 2.
2. Interaction between pin and hole is not only modelled with a normal bearing load, but also with a through-thickness friction having a friction coefficient taken equal to 0.25, based on the testing by Mottram (2005) to account for the FRP/steel contact.
3. Residual thermal stresses resulting from the pultrusion thermal-induced and cure-induced shrinkage processes are not considered. Chen *et al*. (2001) and Zhang *et al*. (2004) developed micro-mechanical models that have been successfully employed in computational analysis and showed that initial residual stresses within pultruded structural shapes dissipate over time owing to viscoelastic creep relaxation (Bank 2006).

Material Properties

This section describes the physical and mechanical properties of the original material used in the extensive testing programme by Matharu (2014). The pultruded material is from the Pultex®

SuperStructural 1525 series of 'off-the-shelve' shapes. Identifier 1525 means the thermoset polyester matrix is Class 1 Flame Retardant. The E-glass FRP fibre architecture consists of mat layers interspersed with nominally constant thickness layers of UniDirectional (UD) rovings having a fibre volume fraction of 60%. The mat reinforcement is type E-TTXM 4008, a Triaxial Stitched Fabric Mat (TSFM) from Vectorply Corporation (http://vectorply.com/wp-content/uploads/2015/06/E-TTXM-4008.pdf). The pultruded shape has an outer (relatively thin at 0.03 mm (see Table 1)) surface veil (non-structural) for UV protection and a barrier to moisture diffusion. The NEXUS® veil layer is resin-rich, non-structural and consists of randomly orientated short 100% melt polyester fibres, which has a mass per unit area < 100 g/m^2.

As seen in Fig. 2 there are five alternating layers of UD and TSFM, with two TSFM layers at mid-thickness having no UD layer between them. TSFM is of a stitched continuous fabric having four layers with the lay-up sequence of +45°/90°/–45°/random chopped strand. Assuming the volume fraction of fibres in the continuous layers is 60% the chopped strand backing layer in TSFM has a volume fraction of 16%. The thicknesses of the layers are 0.35 mm for the 90^o, 0.51mm for the ±45^o and 0.54 mm for the chopped strand. It is known from Creative Pultrusions Inc. that the UD layers comprise of 56 yield rovings.

The thermoset resin is the Reichhold 31031 unsaturated isophthalic polyester resin. To produce a matrix for the pultrusion composite processing there are additives and fillers. The largest proportions in the formulation, which consist of 13 constituent parts, is for the polyester resin, at approximately 80% of the bulk matrix.

A series of resin burn-off tests were conducted by Matharu (2014) to estimate the volumetric proportions of UD and TSFM fibres, and matrix, as well as to establish the nominal thicknesses of each layer. The resin burn-off procedure was adapted from the method described in Appendix B of the PhD thesis by Lane (2002), and with reference made to the testing procedure given in Ye *et al*. (1995) and ASTM D2584-11 (2011). Table 1 summarizes the results from the resin burn-off tests. Because the reinforcing effect of the Surface Veil (SV) layers is minimal it can be seen that the total amount of glass fibre with the two main reinforcing laminae of UD and TSFM are equal at 34% volume fraction. The volume percentages of UD, TSFM and matrix are in the range 30 to 34. The final row in Table 1 reports the nominal thicknesses of the layers (the t_{lay}s) on the assumption that they are constants for a particular reinforcement type in the original material. Note that both the veil and TSFM thicknesses are predetermined by their construction. Only the UD layers have a freedom to have a processing variation for layer thickness.

The mechanical properties presented in Table 2 are defined with respect to the local co-ordinate system, with: 1 for the pultrusion direction; 2 for the in-plane direction normal to the direction of pultrusion; 3 for the through-thickness direction. In the literature the direction of pultrusion is often referred to as the longitudinal (or length-wise) direction and the perpendicular (in-plane) direction as the transverse (cross-wise) direction. Notation f_1 is therefore for the in-plane longitudinal strength, f_2 for the in-plane transverse strength, $f_{1,\text{S}}$ for the in-plane shear strength, and $f_{2,\text{S}}$ for the transverse shear strength. Values in the table for Tensile (T) and Compressive (C) actions are for in-plane strengths.

The determination of the elastic constants for the three different laminae are reported in Table 2 was carried out using micromechanical modelling with volume fractions of the constituents established by using the resin burn-off method, as described in Lane (2002). In making the micromechanical modelling calculations, it is assumed that the densities of matrix and glass fibres are 1.1 g/cm^3 (Reichhold, 2006) and 2.56 g/cm^3 (Hancox and Mayer, 1994), respectively. The modulus of elasticity for the matrix constituent is assumed to be 3.2 kN/mm^2 (Reichhold, 2006) and for the fibres it is taken as 72 kN/mm^2 (Hancox and Mayer, 1994). The constituent Poisson's ratios are assumed to be 0.36 and 0.22, respectively. Using the rule of mixtures approach with the two lamina stiffnesses in Table 2 predictions for the elastic constants of the 9.6 mm thick panel are E_1 = 25.0 kN/mm^2, E_2 = 16.7 kN/mm^2, G_{12} = 4.5 kN/mm^2 and ν_{12} = 0.36. These elastic constants are seen to be different to the tabulated properties of E_1 = 21.3 kN/mm^2 and E_2 = 9.6 kN/mm^2 in the Design Manual from Creative Pultrusions (2016). The Design Manual stiffnesses are for a range of pultruded shape sizes and the larger the size is, the lower can be the volume proportion (and maybe fibre volume fraction) of the unidirectional reinforcement. As a consequence of this fact the tabulated moduli of elasticities are for minimum measured from all the shapes in the series range. Because the published stiffnesses are for the whole 1525 series they are less reliable, and this is the engineering reason why the micromechanical modelling laminae stiffnesses in Table 2 are input data for the FE analyses. The web material consists of alternative reinforcing layer of UD and the TSFM having a balanced lay-up, comprising TSFM1 layer at 1.38 mm thickness, UD1 at 1.93 mm, TSFM2 at 1.42 mm, TSFM3 at 1.39 mm, UD2 at 2.01 mm and TSFM4 at 1.47 mm. Note that mid-thickness layers TSFM2 and TSFM3 do not have UD reinforcement between them. Accounting for experimental errors in the resin burn-off testing the thickness of the four TSFM layer can be taken to be constant at 1.4 mm. The UD layers have a nominal constant thickness of 2.0 mm.

The strengths listed in the middle column in Table 2 are for the laminate. PFRP materials having the individual fibre reinforcement types (and the same matrix) are not pultruded and so their strength (and stiffness) properties cannot be measured. Matharu (2104) conducted a series of tension and compression coupon tests (in batches of 10) to determine the panel's in-plane strengths. The longitudinal (compression) strength ($f_{1,\mathrm{C}}$) for the batch ranges from 280 to 328 N/mm^2, whereas $f_{2,\mathrm{C}}$ is found to range from 99 to 153 N/mm^2. The mean longitudinal strength in tension ($f_{1,\mathrm{T}}$) at 294 N/mm^2 is 4% lower than the mean compression, whereas the transverse tensile strength ($f_{2,\mathrm{T}}$) is, as expected, much lower, at 63% of the compression mean of 133 N/mm^2. The mean in-plane shear strength $f_{1,\mathrm{s}}$ is 91 N/mm^2 was taken from D'Alessandro (2009). In the FE work the transverse shear strength ($f_{2,\mathrm{s}}$) is taken to be $f_{1,\mathrm{s}}$.

Each (continuum) damage evolution law includes a corresponding fracture energy (or fracture toughness), G_c, that governs crack growth for the modes illustrated in Fig. 1. Fracture energy is defined as the work needed to create a unit area of a fully developed crack. Guidelines for the evaluation of these fracture properties can be found in Pinho *et al*. (2006) and Maimi *et al*. (2007). The four values adopted in this study are listed in the last column in Table 2. They were not experimentally determined, but estimated based on research expertise and data available from the literature (Kelly and Zweben 2000; Girão Coelho *et al*. 2015).

The assumed modelling inputs for interfacial mechanical properties are summarized in Table 3. To establish the peak strengths f_{I} and $f_{\mathrm{II}} = f_{\mathrm{III}}$ for Eq. (1), in the absence of experimental measurements, the in-plane strengths $f_{2,\mathrm{T}}$ and $f_{1,\mathrm{S}} = f_{2,\mathrm{S}}$ were factored down by adopting a weakening factor f_{w}, according to guidance from the failure criterion work by Puck and Schürmann (2002), see Knops (2008), and from the computational modelling work by Wimmer *et al*. (2009). The critical normal interface traction (for opening mode) of the cohesive zone elements is therefore assumed to be equal to the transverse tensile strength, $f_{2,\mathrm{T}}$, times the weakening factor. The critical shear interface tractions (for sliding and tearing modes) are both assumed to be equal to the shear strength, $f_{2,\mathrm{S}}$, times the same weakening factor.

It was found in a sensitivity analysis from a series of FE simulations that the overall response for $f_{\mathrm{w}} = 0.25$ gives the one closest to the pin-bearing experimental results from Matharu (2014). With $f_{\mathrm{I}} = 21$ N/mm^2 and $f_{\mathrm{II}} = f_{\mathrm{III}} = 23$ N/mm^2 the analysis indicates a relatively weak interface between the laminae, as defined by the FE modelling data given in Fig. 2 and Table 2. A similar f_{w} has already been proposed by Girão Coelho *et al*. (2016) for this same pultruded material when analysing the different structural engineering problem of delamination failure in a pultruded leg-angle shape subjected to tying force, as would be found in a web clip connection between beam and column members.

The piecewise linear traction-separation law of the cohesive elements is described according to the lamina strength presented in the last column in Table 2. Using the guidance from Camanho *et al*. (2003) the elastic stiffnesses (per unit area) of the interface (K_{I}, K_{II} and K_{III} associated with f_{I}, f_{II} and f_{III}) are assumed to be equal to 10^6 N/mm^3. For modes I, II and III illustrated in Fig. 1 the critical energy release rates of $G_{\mathrm{I,c}}$ and $G_{\mathrm{II,c}} = G_{\mathrm{III,c}}$, were taken as 0.2 (200) and 0.5 (500) N/mm (J/m^2), respectively (Girão Coelho 2016).

Description of the Model

Defined in Fig. 2 are the dimensions for the pin-bearing specimen that is to be modelled and analysed. Each plate of 9.6 mm thickness (t) is 80 mm long (e_1) and 80 mm wide (w). The pin diameter (d) is set equal to 11.8 mm for M12 and to 19.8 mm for M20 steel bolting, while the hole diameter (d_0) was taken 2.4 mm larger, based on practical dimensions. This allowed for the maximum clearance hole tolerance size (Anonymous 2012) and the shaft diameter to be identical to the bolt diameter specification. The pin was placed centrally in the hole, which itself is mid-positioned in the top surface. The UD layers are oriented with the fibres aligned to the direction of the bearing load.

The FE model is constructed from stacked continuum shell elements with the individual UD and TSFM layers being modelled separately. Although the element SC8R possesses the geometry of a brick, its kinematic and constitutive behaviour is similar to those of conventional shell elements (Abaqus 2016). The continuum shell elements are able to reproduce reliable results in simulations of thin-walled laminated structures by means of only one element in a lamina thickness, owing to a higher-order displacement field (Parisch 1995; Remmers *et al*. 2003). Cohesive interface elements are used to connect together an TSFM and an UD layer to allow for (multi-)delamination failures to occur. As shown in the diagram in Fig. 2 four cohesive interfaces I1 to I4 are modelled. Justification for no cohesive interface between the two touching TSFM layers at mid-thickness is that Matharu (2014) did not observe, after tests, delamination failure over this interface.

The in-plane mesh geometry for the interfaces had to be the same as that for the laminae. A typical mesh with its very refined mesh specification is illustrated in Fig. 3, where adjacent to the hole a finer mesh is used to correctly capture delamination and the important contact situation. Note that using mirror symmetry about the two TSFM layers at mid-thickness the mesh is for a thickness of 4.8 mm (or $t/2$). The thickness of interface layers I1 and I2 are $10^{-3}t_{lay}$, based on the 1.4 mm TSFM layer thickness. Element size was increased towards the plate edges to reduce calculation time. The FE mesh specification in our study of the original material has a total of 27834 (M12) continuum shell SC8R elements (or 32520 elements for the M20 specimen), and 18556 COH3D8 cohesive elements (M12 and two interfaces) (or 21680 elements for M20 specimen and two interfaces). Interfaces I1 and I2 (or I3 and I4) are included in the FE model.

As mentioned earlier the (steel, smooth shafted) pin is modelled as a three-dimensional analytical rigid body revolved shell.

Loading of the specimen is simulated by displacing the bottom edge against the fixed pin as indicated by the ‘load’ arrows in Fig. 2. Vertical deformation is resisted by the contact surface for pin and hole perimeter at the top of the specimen. Contact behavior is modelled with the ‘hard’ surface-to-surface contact formulation in the normal direction and the friction is modelled using an isotropic friction model with a coefficient of 0.25. Note that the coefficient of friction was not measured (Mottram 2005) for the steel-FRP contact in the through-thickness direction. This represent one of several modelling data assumptions made to complete a successful FE simulation and they have been reported in this paper.

The Abaqus implicit analysis is run with the laminae properties listed in Tables 2 assigned to the appropriate UD or TSFM layers and with the interfacial properties in Table 3. For each lamina the Hashin failure criterion (Hashin 1983) is used to predict damage onset (Girão Coelho 2016), and because interfacial delamination failure always occurs first this criterion is of secondary importance. To account for damage progression after crack initiation there is a fracture energy calculated for each of four failure modes using the fracture energies in Table 2 (Girão Coelho *et al*. 2015). To assist with numerical convergence of the Abaqus solver the authors used previous simulation ouputs (Girão Coelho *et al*. 2015) to set a global stabilization factor to 2×10^{-4}.

Modelling Strategy Validation

Results from static analyses are compared with maximum pin-bearing loads from experiments. In the series of tests a specimen's stiffness was not measured because it had no meaning to the aim of the strength investigations in Matharu's PhD work (2014), which were to establish characteristic values for pin-bearing strengths. In this paper the web material studied by Matharu is referred to as the original (non-aged) material.

One finding from the FE simulations is that delamination failure always governs the magnitude of the load for pin-bearing strength and this matches experimental observations. As a direct consequence the relevant Hashin parameters were found to be always below 1.0. This shows that it has been acceptable for the authors to have made the approximate assumption that the laminate strengths in Table 2 could be taken to be the individual laminae strengths. The pin-bearing strength, here expressed in terms of applied load, is reached when there is extensive delamination growth at the two interfaces (I1 and I2), and there is a sudden load drop-off during the displacement controlled loading. Fig. 4 is for plots constructed from Abaqus outputs of load (kN) versus the axial displacement (mm) in the bearing force direction. The grey shaded circle symbols are for numerical results with the larger black filled circle at the load when initiation of delamination fracturing is numerically predicted. In the legend there is (I1) to identify that the critical delamination is at Interface 1, its location is defined in Fig. 2. The batch test results from Matharu (2104) are reported by three representative loads. The batch mean is given by the solid horizontal line, and the maximum and minimum specimen loads are given by the upper and lower dashed lines. The load range between the two dashed lines gives the measured variation from testing a batch of 10 nominally identical specimens. The coefficient of variation for the pin-bearing strength (Matharu 2014) for the M12 batch is 10.4 and for the M20 batch is 8.8%.

Fig. 4(a) is for the M12 pin, and using the same axis scales the equivalent computational results for the M20 pin are reported in Fig. 4(b). The predicted load-displacement response is seen to start off linear, and progress with non-linearity above 15 kN for M12 and 22 kN for M20. The computational response is seen to differ from the virtually linear load-stroke relationship recorded by the testing machine. Above the loading (defined by filled circle symbol) for delamination initiation there is a reduction in structural stiffness and the load-displacement response softens with progressive delamination growth, before ultimate failure. Stiffness degradation after delamination initiation and progressive growth is not an outcome in testing since delamination onset is believed to occur at the same instance the peak load is reached. Importantly, should the FE modelling methodology presented herein be used to aid the design of bolted connections the predicted load for delamination initiation is useful because as Figs. 4(a) and 4(b) show it is below the lower bound test result.

Returning to the information in Fig. 4, the peak (Abaqus) loads of 23 kN (Fig. 4(a) for M12) and of 35 kN (Fig. 4(b) for M20) compare favourably with the mean experimental loads (Matharu 2014) of 22 kN and 34 kN, respectively. The predictions are in very good agreement with computed strengths only 4.5% and 6% higher. The positive correlation shown by the results in Figs. 4(a) and 4(b) for two independent batches provides good validation for applying the FE modelling approach to determine pin-bearing strengths.

In Fig. 5 the deformed shape is shown at peak load (magnification factor is 2.5). Fig. 5(a) is for the M12 pin and the maximum load of 23 kN, whereas Fig. 5(b) is for the M12 pin at maximum load of 36 kN. In both parts the deformations clearly shows the typical ‘brooming’ for compression induced delamination failure at interfaces I1 (nearest) and I2 (farthest).

Inspection of the localised through-thickness deformation in Fig. 5 helps to explain why delamination failure is the mechanism that governs the pin-bearing strength. Under the increasing pressure from the bearing (rigid) pin the existence of Poisson’s ratio effect is for the laminate to need to expand freely in the through-thickness direction. This physically cannot happen because of the friction restraint over the steel pin/FRP contact area and the volume of the surrounding FRP material resisting the bearing load. As seen in Figs. 5(a) and 5(b) the deformation is in the form of a bulge with a short wavelength ($\cong 0.44d_0$). A complex, through-thickness stress field with tension (in the z-direction) is generated local to the hole perimeter, and within the influence of the bulge zone.

It can be speculated that when the maximum through-thickness tensile stress reaches f_I, or the limit given by Eq. (1) when f_I interacts with f_{II} and f_{III} there will be cohesive failure for initiation of delamination failure. Propagation of a delamination crack to the final size shown, for example, in Fig. 6 is numerically controlled by fracture mechanics (Girão Coelho 2016) and the energies listed in Table 3.

The contour plots presented on interface surfaces in Fig. 6 show that, at maximum load, delamination fracturing at the two interfaces has progressed from the hole into the body of the specimen. Fig. 6 parts (a) and (b) are for the M12 and M20 bolt diameters, respectively. Damage progression can be tracked, from 0 (none) to 1 (complete), using the Abaqus output parameter Stiffness DEGradation (SDEG), which indicates the state of damage in the cohesive elements and thereby provides insight into damage initiation and propagation. The red coloured area (SDEG is 0.7 to 1.0) is for complete interface separation and the thin (green coloured) zone around the damage zone's perimeter is for partial damage (SDEG is 0.3 to 0.7). Where the material on the interface surface is coloured dark blue there is no damage (for SDEG < 0.3), with full continuity across the interface. Interface I1 is on the left-side and interface I2 on the right-side. One observation from the contouring presented in Fig. 6 is that the delamination damage has progressed from an initial state with a stable crack front; this is evidence for bearing failure offering the bolted connection a level of damage tolerance.

Overall, we find that the predicted delamination cracks are fairly repeatable and overall are representing the visual observations of bearing surface cracking made by Matharu (2014). The numerical results presented in Figs. 4 to 6 demonstrate the ability of the FE modelling methodology to appropriately predict the pin-bearing mode of failure where interaction between intralaminar and interlaminar modes is strongly coupled.

Changing the Bearing Strength for Bolted Connections

It is well-known that by increasing the size of the clearance hole the bearing strength decreases (Yuan *et al*. 1996). Figs. 7 and 8 are equivalent to Figs. 4 and 6. In Fig. 7 there are two further load-displacement results for clearance holes of 0 mm (tight fitting) and 1.6 mm (without fabrication tolerance (Anonymous 2012)). Although there is a gain in delamination initiation and maximum loads on reducing clearance from 2.6 to 1.6 mm, there is a significant increase in their values, at 48% (M12) and 39% (M20), for the no clearance situation. Even the change in load on having the clearance equal to the nominal design guideline of 1.6 mm (Creative Pultrusions 2016; Strongwell 2016) justifies why testing for the characteristic strength (Mottram and Zafari 2011; Matharu 2014) has to be with the maximum practical clearance. Illustrated in Fig. 8 are the delamination zones for no clearance and the maximum loads of 25 kN for M12 (Fig. 8(a)) and of 37 kN for M20 (Fig. 8(b)). By inspection it can be seen that the shape of the delamination cracks at interfaces I1 and I2 are broadly similar to those in Figs. 6(a) and 6(b) when the clearance hole is 2.6 mm. Because the tight fitting situation generates pressure over the whole semi-circular notch there is interfacial failure in the laminate beyond the boundary of the hole. This finding shows that the test method applied by Matharu (2014) will not give the actual pin-bearing strength if it is practical on- or off-site to assemble a bolted lap-joint with no hole clearance. By applying our FE modelling approach it is feasible to establish the clearance size at which the delamination growth at peak load first goes beyond the confines of the bolt hole perimeter.

Keeping all other parameters constant to those in Matharu's testing, the next change to be evaluated by a sensitivity analysis is the relative thicknesses of the UD and TSFM layers (for a constant specimen thickness (t) of 9.6 mm). For both bolt diameters Table 4 reports the numerical results of: elastic stiffness (S_{el}); pin-bearing load for initiation of delamination ($R_{br,ID}$); maximum pin-bearing load ($R_{br,max}$); the two load ratios of $R_{br,ID}/R_{br,max}$ and $R_{br,max}/R_{br,max,baseline}$, where $R_{br,max,baseline}$ is the maximum pin-bearing load for the original material (i.e. 23 and 36 kN for M12 and M20, respectively). The original material's predictions are presented in the first row of numbers, with three parametric variations given in the next three rows. The percentage of TSTM in t is 58% in the original material and ranges from 42 to 67% in the three sensitivity analysis materials. As expected, S_{el} increases as the UD percentage increases. Combining the M12 and M20 pin results it is found that neither $R_{br,ID}$ nor $R_{br,max}$ show any definite trends. $R_{br,max}$ is seen to remain virtually constant at 23-24 kN (M12) or 35-36 kN (M20). These observations are highlighted by the virtually constant load ratios for the two bolt sizes.

The next study investigates the effect of changing the thickness of the mid-thickness TSFM. One reason for this parametric study is that the maximum load is governed by delamination failure at interface I1, not I2 that is for the outer interfaces of the mid-thickness mat layer. The presentation of information and computed predictions in Table 5 is the same as in Table 4. The parameter change is given in the second column where the thickness of the mid-thickness TSFM reduces in four increments to $0t_{orig}$ from its original specification of 2.8 mm ($1.0t_{orig}$). The loss in the thickness of the middle TSFM is replaced by UD reinforcement, shared equally by the two equal-thickness UD layers. One observation is that the material with $0t_{orig}$ and the M12 pin has the highest $R_{br,ID}$ at 21 kN. With the M20 bolt size the highest $R_{br,ID}$ of 33 kN is for $0.15t_{orig}$. There is, again, not a significant change in $R_{br,max}$ with the parametric variation, which for M12 is either 23 or 25 kN, and for M20 is 36, 37 or 38 kN.

Note that the delamination contours for the specimens covered in Tables 4 and 5 were found to be similar to those shown in Fig. 6. They are not reported in this paper because of lack of space.

Returning to the original study parameters (Matharu 2014), the next variable to be examined is reversing, in the laminate, the stacking sequence of layer TSFM1 or layer TSFM2 or of both. In the original material interfaces I1 and I2 had UD fibres on one side and +45° fibres from TSFM on the other side. By reversing the TSFM layer the interface has UD and chopped strand fibres in contact. Information in Table 6 follows Tables 4 and 5 with the stacking sequence changes given in the second column. The results are difficult to interpret with little change in predictions with the M12 pin and a significant increase to 1.16 in ratio $R_{br,max}/R_{br,max,baseline}$ when the larger M20 pin is employed.

In the 1990s the wide flange shapes (Mottram and Zafari 2011) from Creative Pultrusions Inc. (2016) did not have a triaxial mat reinforcement. Prior to introducing the Pultrex® SuperStructurals product range the mat reinforcement was an CSM, having a local glass fibre volume fraction of ≅23%. For the next study the material has either TSFM or CSM for the mat reinforcement. For these simulations the model did not have the mid-thickness mat reinforcement. Predictions are presented in Figs. 9 and 10 in the usual way. In the plots in Fig. 9 the load-displacement response for the original laminate (Matharu 2014) is given by the shaded filled circle symbols. Superimposed on this curve are the predicted results when the TSFM is fully replaced with CSM. The higher pair of curves in Figs. 9(a) and 9(b) is for the situation where the mid-thickness mat is replaced by UD reinforcement, thereby increasing S_{el}. A difference observed is that the maximum load is slightly higher with the 'older' mat reinforcement and it occurs at a higher axial displacement. The positions of the open unfilled circle for the load at delamination initiation show that another difference on having CSM reinforcement is that failure is delayed by about 2 kN (M12) or 4 kN (M20). A key finding is that the maximum loads are the same at 25 kN (M12) and only slightly different at 38 and 40 kN (M20) after replacing the TSFM with CSM. An important conclusion from this study is that the presence of ±45^{o} fibres in the TSFM layers has not increased the pin-bearing strength.

What is observed from looking at the contour plots in Figs. 10(a) and 10(b) for delamination growth at maximum load is that the shape of the fractured zone is much more centrally located and goes further into the specimen when the mat reinforcement is CSM. The area associated with partially damaged material is seen to be larger too. These figures show that the size and shape of a delamination crack will depend on the orientations of the fibres in the two layers adjacent to the failed interface.

The final two FE simulations were performed to find out if pin-bearing strength increases when the chopped strand backing in the TSFM layer is replaced by proportional increases in the 90^{o} and

±45° fibre reinforcements. The rationale for this parametric study is that the chopped strand layer has a relatively low fibre volume fraction at 16% and occupies 39% of the TSFM's 1.4 mm thickness. The predicted results are reported in Figs. 11 and 12. As observed from the two curves in Fig.11 there is little difference in the response up to when delamination failure initiates. Perhaps, unexpected it is found that the original TSFM with the chopped strand backing has the higher maximum load for both M12 (i.e. 23 and 18 kN) and M20 pins (i.e. 35 and 29 kN). Comparing the equivalent contour plots in Fig. 12 with those presented in Fig. 6 it is seen that shape and size is dependent on the fibre reinforcement local to the failing interface.

Results for this, and other parametric studies reported in this paper have shown that pin-bearing strength can be highest when the mat reinforcement has random continuous or chopped fibres at the relatively low volume fraction of < 25%.

Concluding Remarks

A FE modelling methodology using Abaqus software, without customized user-subroutines, has been formulated that can be employed in parametric and/or sensitivity analyses to determine the pin-bearing strength of laminated composite materials. Numerical outputs are able to predict the initiation and growth of delamination failures that governs what a pin-bearing strength is. Using batch test results for a 9.6 mm thick web from a pultruded structural shape the simulation results for the two pin diameters of 12 and 20 mm are shown to give good strength predictions. To assist designers of bolted connections an interesting finding is that initiation of delamination cracking is not at the peak load, and that this predicted load is close to, yet below the lowest pin-bearing strength measured from a batch of 10 specimens. There was, however, no observable evidence that there was stable delamination failure(s) during testing before the pin-bearing strength load was reached. Although this finding shows that the computational solution differs from the actual pin-bearing response an important finding is that the FE modelling methodology can reliably establish the ultimate failure load for pin-bearing failure.

To demonstrate the potential of applying the modelling approach to investigate how the pin-bearing strength might vary with parameter changes a number of parametric studies are presented. While maintaining constant the other parameters in the test series, numerical predictions are reported for changing the: clearance hole size; relative thickness of the unidirectional and triaxial mat layers; thickness of the mid-thickness triaxial mat layer; stacking sequence of the triaxial mat layer; triaxial mat to a continuous strand mat; triaxial mat's construction so that the 39% thickness of chopped strand backing is replaced proportionally with reinforcement having the orientations of $\pm 45^{o}$ and 90^{o}.

The main findings from the numerical results can be summarized as follows. New understanding is obtained from contour plots for the Abaqus output Stiffness DEGradation showing the size and shape of delamination failure(s) over interfaces. As expected, pin-bearing strength is found to increase with reduced hole clearance and is significantly higher (at 48% and 39% for the two pin diameters) when there is no clearance. Under the tight fitting condition it is observed that the test method (Matharu 2014) becomes invalid because, at peak load, delamination failure is not contained within the semi-circular hole. A less expected finding is that the strength is not sensitive to the relative thicknesses of the unidirectional and mat layers, and there is no benefit on having replaced the continuous strand mat with a triaxial mat (which is more expensive). Furthermore, tabulated results from parametric studies do not offer obvious trends, and the authors cannot give any scientific explanation to why computed results are seen to be highly dependent on the pin diameter being either 12 or 20 mm. The final study shows that strength is reduced on replacing the chopped strand backing in the triaxial mat layers; the opposite might be expected since the additional $\pm 45^{o}$ fibres ought to be effective in resisting a higher bearing load.

The satisfactory performance of the computational predictions in determining the response at peak load encourages the authors to recommend that the Abaqus modelling methodology may be used to: (i) design the laminate (produced by the pultrusion composite processing method) for a specified pin-bearing strength; (ii) predict the pin-bearing strengths for bolted connections having parameters to be scoped in a structural design standard.

References

Abaqus [Computer Software], "*ABAQUS Unified FEA – Complete solutions for realistic simulation*," Version 6.14, Dassault systems, http://www.3ds.com/products-services/simulia/products/abaqus. (last assessed 01/08/2016)

Anonymous. (2012). '*Code of standard practice for fabrication and installation of pultruded FRP structures*,' ANSI standard, American Composites Manufacturers Association, 1st Edition, Arlington, VA..

Anonymous. (2016). "*Fiberglass pedestrian and trail bridges*, E. T. Techtonics, Alum Bank, PA, USA. http://www.ettechtonics.com/ (accessed 01/08/2016)

ASTM (American Society for Testing and Materials). (2011). "Standard test method for ignition loss of cured reinforced resins." *D*2584-11, West Conshohocken, Pennsylvania, U.S.A.

Bank, L. C. (2006). *Composites for construction: Structural design with FRP materials*, John Wiley & Sons, New Jersey, U.S.A.

Benzeggagh, M. L, and Kenane, M. (1996). "Measurement of mixed-mode delamination fracture toughness of unidirectional glass/epoxy composites with mixed-mode bending apparatus." *Compos. Sci. Technol.*, 56, 439–449.

Brewer, J. C, and Lagace, P. A. (1988). "Quadratic stress criterion for initiation of delamination." *J. Compos. Mater.*, 22, 1141–1155.

BS EN 1993-1-1:2005. "*Eurocode 3 - Design of steel structures - Part 1-1: General rules and rules for buildings*," British Standards Institution (BSI), London.

Camanho, P. P., Dávila, C. G., and Moura, M. F. (2003). “Numerical simulation of mixed-mode progressive delamination in composite materials.” *J. Compos. Mater.*, 37(16),1415–1438.

Creative Pultrusions. (2016). The New and Improved Pultrex1 Pultrusion Design Manual (Imperial Version, Volume 5 Revision 2). Creative Pultrusions, Inc., Alum Bank, PA, USA. http://www.creativepultrusions.com/index.cfm/products-solutions/fiberglass-standard-structural-profiles/pultexc2ae-pultrusion-design-manual/ (accessed 01/08/2016)

Chen, Y., Xia, Z., and Ellyin, F. (2001). “Evolution of residual stresses induced during curing processing using a viscoelastic micromechanical model.” *J. Comp. Mater.*, 35(6), 522–542.

D'Alessandro, R. G. (2009). “*Characteristic values of mechanical properties of wide-flange pultruded FRF beams*,” MSc Thesis, University of Wisconsin-Madison, USA.

Du, A., Liu, Y., Xin, H. and Zuo, Y. (2016). “Progressive damage analysis of PFRP double-lap bolted joints using explicit finite element method,” *Comp. Struct.*, 152, 860–869.

Falk, M. L., Needleman, A., and Rice, J. R. (2001). “A critical evaluation of cohesive zone models of dynamic fracture.” *J. Phys. IV*, Proc 11(Pr.5), 43–50.

Girão Coelho, A. M. (2016). “Finite element guidelines for simulation of delamination dominated failures in composite materials validated by case studies.” *Arch. Comput. Method. E.*, 23(2), 363–388.

Girão Coelho, A. M., and Mottram, J. T. (2015). “A review of the behaviour and analysis of bolted connections and joints in pultruded fibre reinforced polymers.” *Mater. Design*, 74, 86–107.

Girão Coelho, A. M., Mottram, J. T., and Harries, K. A. (2015). “Finite element guidelines for simulation of fibre-tension dominated failures in composite materials validated by case studies.” *Comp. Struct.*, 126, 299-313.

Girão Coelho, A. M., Mottram, J. T., and Matharu, N. (2016). “Virtual characterization of delamination failures in pultruded GFRP angles.” *Compos. Part B – Eng.*, 90, 212–222.

Hancox, N. L. and Mayer, R. M. (1994). “*Design data for reinforced plastics, A guide for engineers and designers*,” Chapman and Hall, London.

Hashin, Z. (1983). “Analysis of composite materials.” *J. Appl. Mech.*, 50, 481–505.

Kelly, A., and Zweben, C. (eds.). (2000). *Comprehensive composite materials*, *vol*. 2, Elsevier Science.

Knops, M. (2008). *Analysis of failure in fiber polymer laminates – the theory of Alfred Puck*. Springer, Germany.

Lane, A. (2002). *An experimental investigation of buckling mode interaction in PFRP columns,* PhD thesis, University of Warwick, U.K.

Maimí, P., Camanho, P. P., Mayugo, J. A., and Dávila, C. G. (2007). “A continuum damage model for composite laminates, part I: constitutive model.” *Mech. Mater.*, 39, 897–908.

Matharu, N. S. (2014). *Aspects of bolted connections for fibre reinforced polymer structures,* PhD Thesis, University of Warwick, U.K.

Mottram, J. T. and Turvey G. J. (2003). ‘Physical test data for the appraisal of design procedures for bolted joints in pultruded FRP structural shapes and systems,’ *Prog. Struct. Eng. Mater.*, 5(4), 195-222.

Mottram, J. T. (2005). “Friction and load transfer in bolted joints of pultruded fibre reinforced polymer section.” *Proc., 2nd Int. Conf. on FRP Composites in Civil Engineering*, R. Seracino, ed., Taylor & Francis, Adelaide, Australia, 845–850.

Mottram, J. T. and Zafari, B., (2011). “Pin-bearing strengths for design of bolted connections in pultruded structures,” *P I Civil Eng-Str B*, 164(5), 291–305.

Ortiz, M., and Pandolfi, A. (1999). “Finite-deformation irreversible cohesive elements for three dimensional crack-propagation analysis.” *Int. J. Numer. Meth. Eng.*, 44, 1267–1282.

Parisch, H. (1995). “A continuum-based shell theory for non-linear applications.” *Int. J. Numer. Meth. Eng.*, 38, 1855–1833.

Pinho, A., Robinson, P., and Iannucci, I. (2006). “Fracture toughness of the tensile and compressive fibre failure modes in laminated composites.” *Compos. Sci. Technol.*, 66, 2069–79.

Puck, A., and Schürmann, H. (2002). “Failure analysis of FRP laminates by means of physically based phenomenological models.” *Compos. Sci. Technol.*, 62, 1633–1662.

Reichhold. (2006), “*DION® 31031-00 Medium-high reactivity pultrusion resin*”, Product Bulletin, Revision date January 2006.

Remmers, J. C., Wells, G. N., de Borst, R. (2003). “A solid-like shell element allowing for arbitrary delaminations.” *Int. J. Numer. Meth. Eng.*, 58, 1701–1736.

Starr, T. (2000). *Pultrusion for engineers*, Woodhead publishing Ltd., Cambridge, U.K.

Strongwell. (2016). Strongwell Design Manual. Strongwell, Bristol, VA, USA. See //www.strongwell.com/ (accessed 01/08/2016).

Turon, A., Dávila, C. G., Camanho, P. P., and Costa, J. (2000). “An engineering solution for mesh size effects in the simulation of delamination using cohesive zone models.” *Eng. Fract. Mech.*, 74, 1665–1682.

Turvey, G.J. (2000). “Bolted connections in PFRP structures.” *Progress in Structural Engineering and Materials* 2(2), 146– 156.

Wimmer, G., Schuecker, C., and Pettermann, H.E. (2009). “Numerical simulation of delamination in laminated composite components e a combination of a strength criterion and fracture mechanics. *Compos Part B-Eng* 40,158-165.

Yuan, R. L., Liu, C. J. and Daley, T. (1996). “*Study of mechanical connection for GFRP laminated structures,*” Proceedings of the 2nd International Conference on Advanced Composite Materials in Bridges and Structures (ACMBS-2), The Canadian Society for Civil Engineers, Montreal, 951-958.

Ye, B. S., Svenson, A. L., and Bank, L. C. (1995). “Mass and volume fraction properties of pultruded glass fibre-reinforced composites.” *Composites*, 26(10), 725–731.

Zafari, B. and Mottram, J. T. (2012). “Effect of hot-wet aging on the pin-bearing strength of a pultruded material with polyester matrix,” *J. Compos. Constr.*, 16(3), 340-352.

Zhang, Y., Xia, Z., and Ellyin, F. (2004). “Evolution and influence of residual stresses/strains of fibre reinforced laminates.” *Compos. Sci. Technol.*, 64, 1613–1621.

Fig. 1. Modes of delamination failure: a) Mode I (*m* = I): opening; b) Mode II (*m* = II): sliding; c) Mode III (*m* = III): tearing.

Fig. 2. Geometry: schematic of plate and pin with applied load and composite lay-up showing locations of four interfaces I1 to I4.

Fig. 3. Typical plate mesh for the evaluation of the (12 mm) pin-bearing behaviour of a pultruded specimen, with the symmetry plane facing backwards.

Fig. 4. Load-displacement plots from implementing the FE model, and comparison with experimental data from Matharu (2014): a) M12; b) M20.

Fig. 5. Specimen deformation at maximum predicted load (plots on deformed structure, magnification factor 2.5): a) M12; b) M20.

Fig. 6. Delamination at interfaces I1 (left) and I2 (right) at maximum predicted load (contour plotting on deformed mesh): a) M12 at 23kN; b) M20 at 36 kN.

Fig. 7. Effect of changing the size of the hole clearance: a) M12; b) M20.

Fig. 8. Delamination at interfaces I1 (left) and I2 (right) at maximum load (plots on deformed structure) when specimen has no clearance hole: a) M12 has maximum load of 25 kN; b) M20 has maximum load of 37 kN.

Fig. 9. Plots to maximum load having mat reinforcement TSFM replaced with CSM (filled markers – TSFM; unfilled markers – CSM): a) M12; b) M20.

Fig. 10. Delamination growth at interface I1 at maximum load for mat reinforcement of TSFM (left-side) or of CSM (right-side): a) M12 has maximum load of 25 kN | 25 kN); b) M20 has maximum load of 38 kN | 40 kN)

Fig. 11. Comparison of original material with a new material when the chopped strand layer in the TSFM is replaced by the continuous fibre reinforcements (filled markers – TSFM; unfilled markers – TSFM without chopped strand layer): a) M12; b) M20.

Fig. 12. Delamination at interfaces I1 (left) and I2 (right) at maximum load when chopped strand layer in the TSFM is not present (plots on deformed structure): a) M12 has maximum load of 18 kN; b) M20 has maximum load of 28 kN

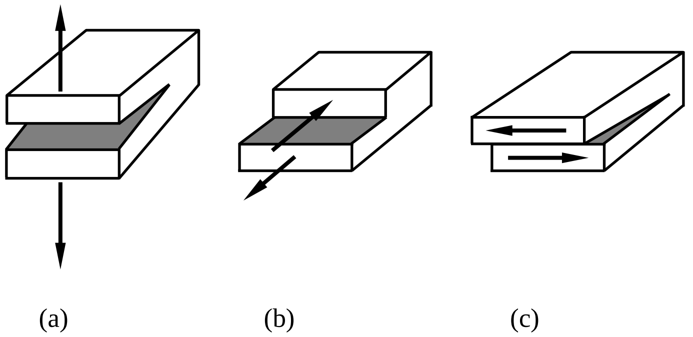
(a)
(b)
(c)

Fig. 1

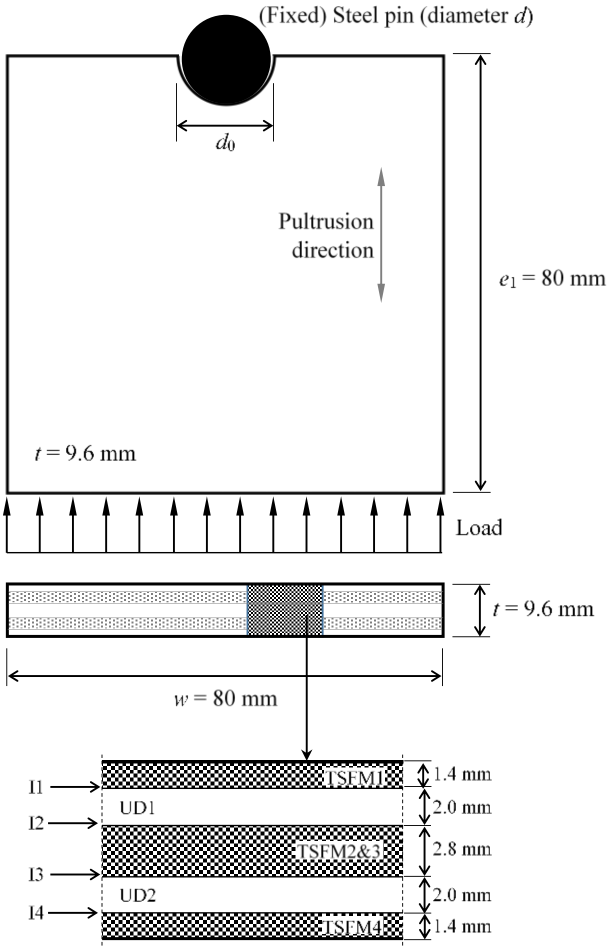
(Fixed) Steel pin (diameter d)
d0
Pultrusion direction
e1 = 80 mm
t = 9.6 mm
Load
t = 9.6 mm
w = 80 mm
I1
I2
I3
I4
UD1
UD2
TSFM1
TSFM2&3
TSFM4
1.4 mm
2.0 mm
2.8 mm
2.0 mm
1.4 mm

Fig. 2

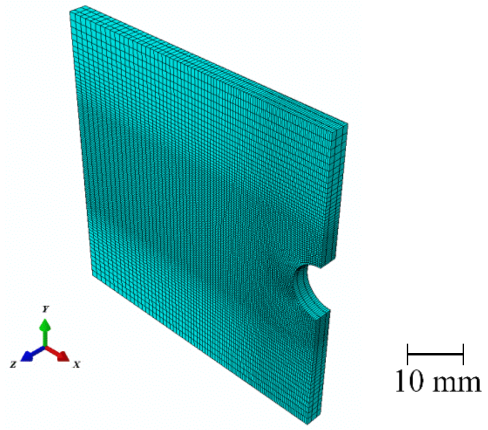
10 mm

Fig. 3

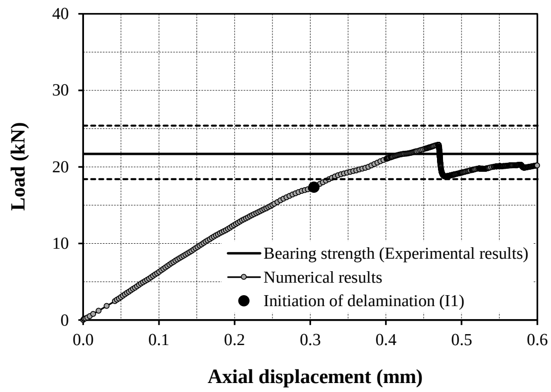
Load (kN)
40
30
20
10
0
0.0
0.1
0.2
0.3
0.4
0.5
0.6
Axial displacement (mm)
Bearing strength (Experimental results)
Numerical results
Initiation of delamination (I1)

(a)

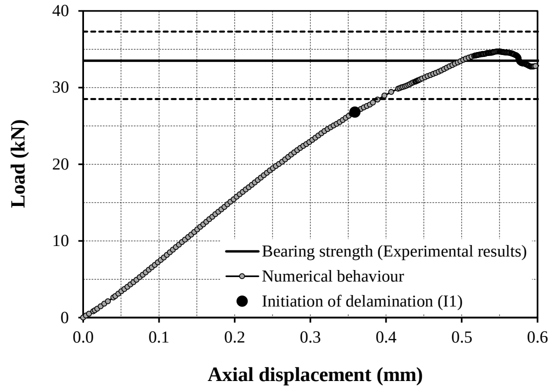
Load (kN)
40
30
20
10
0
0.0
0.1
0.2
0.3
0.4
0.5
0.6
Axial displacement (mm)
Bearing strength (Experimental results)
Numerical behaviour
Initiation of delamination (I1)

(b)

Fig. 4

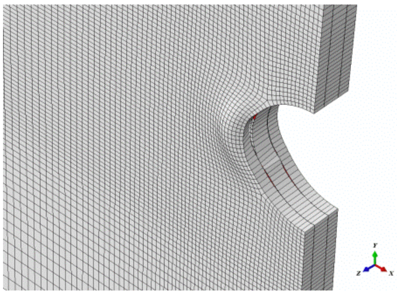

(a)

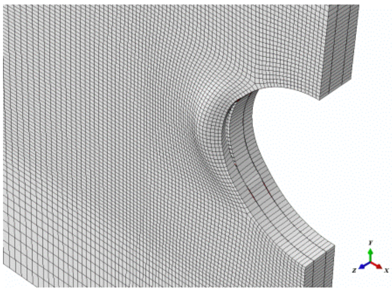

(b)

Fig. 5

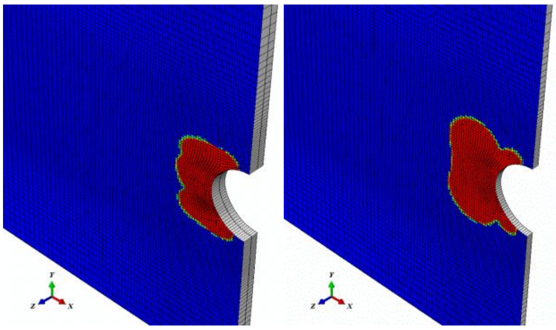

(a)

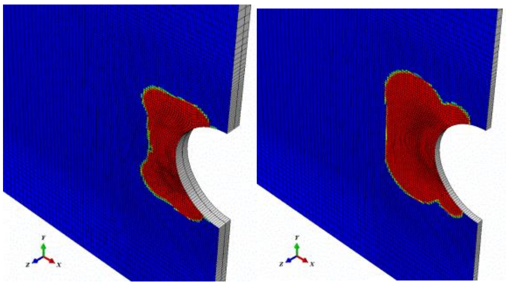

(b)

Completely damaged (0.7 to 1.0) | Partially damaged (0.3 to 0.7) | Undamaged less than 0.3

Fig. 6

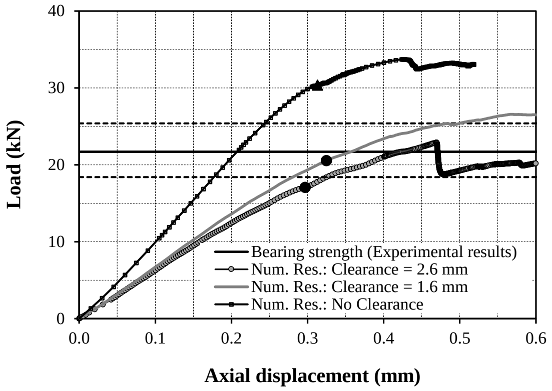

(a)

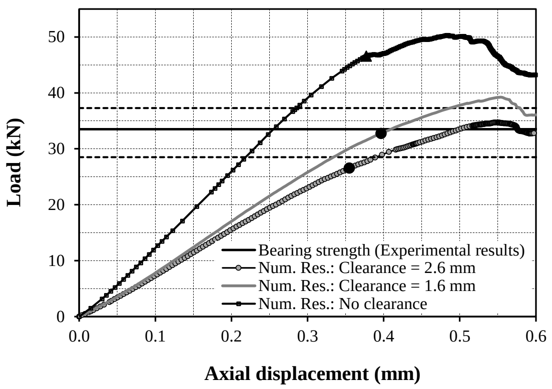

(b)

Fig. 7

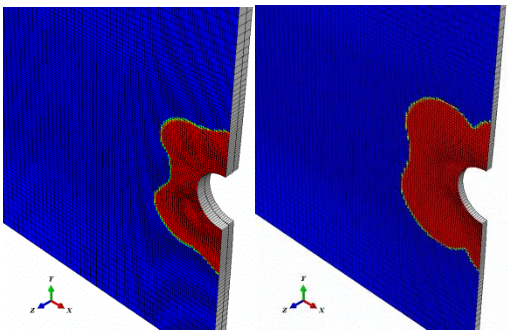

(a)

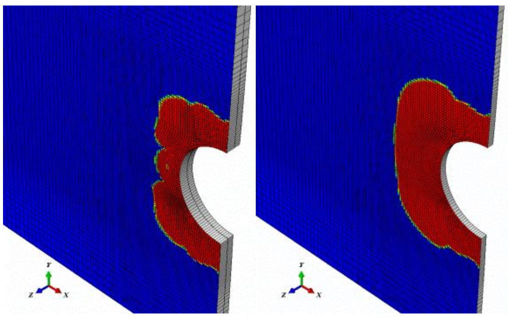

(b)

Completely damaged (0.7 to 1.0) Partially damaged (0.3 to 0.7) Undamaged less than 0.3

Fig. 8

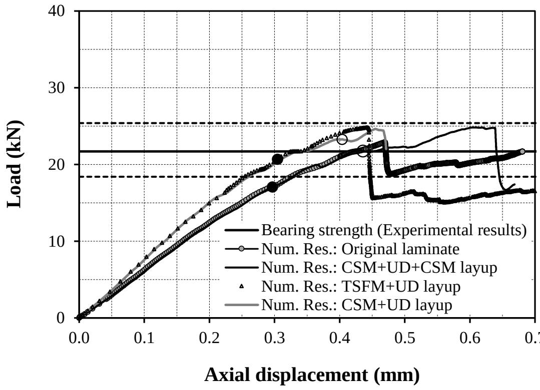

(a)

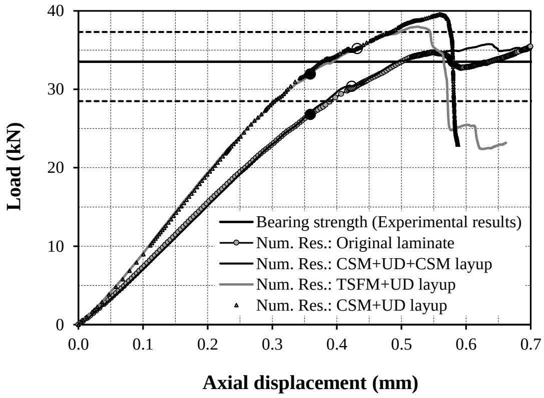

(b)

Fig. 9

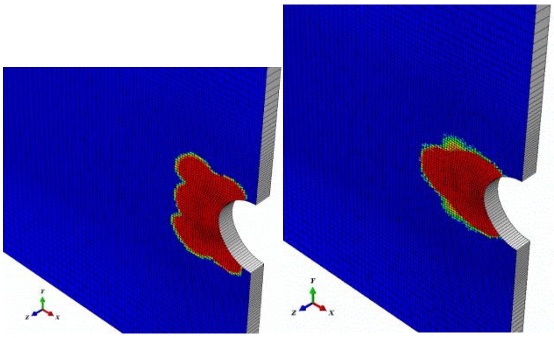

(a)

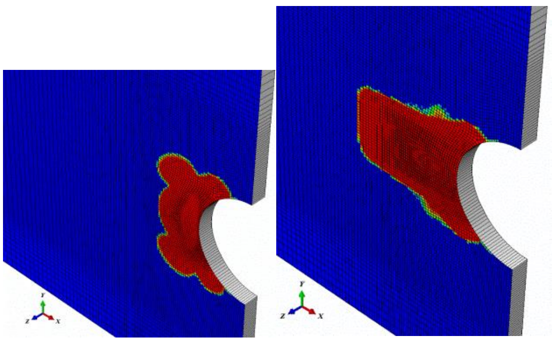

(b)

Completely damaged (0.7 to 1.0) | Partially damaged (0.3 to 0.7) | Undamaged less than 0.3

Fig. 10

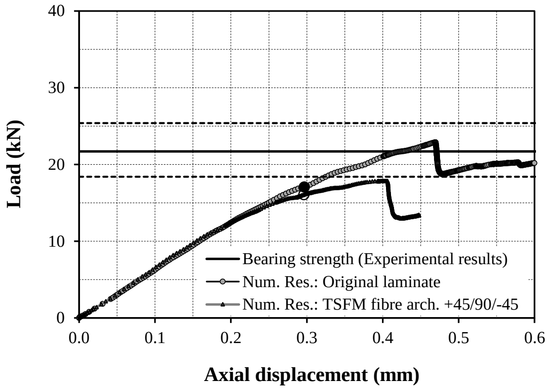

(a)

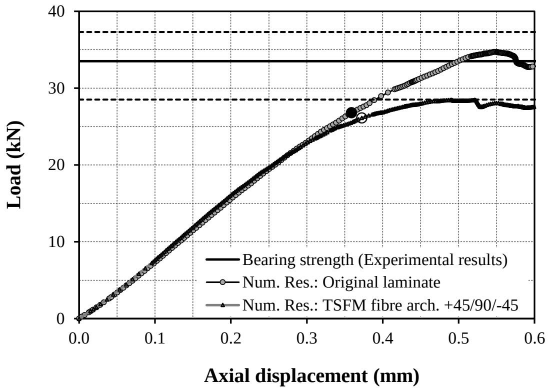

(b)

Fig. 11

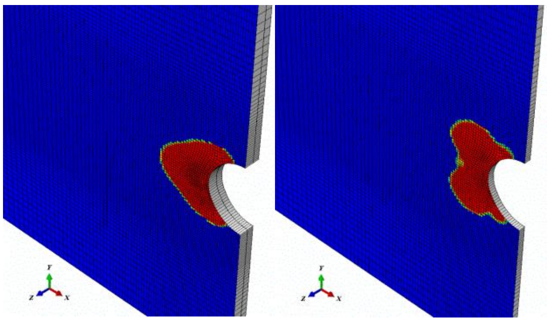

(a)

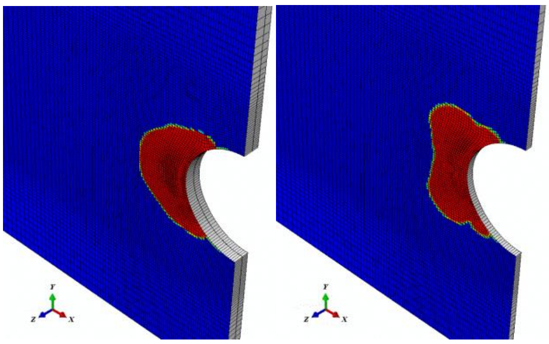

(b)

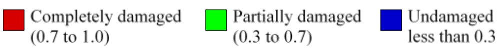

Fig. 12

Table 1. Material constituent properties for the Pultrex® Superstructural material of 9.6 mm thickness.

	Constituent part			
	SV	TSFM	UD	Matrix
Number of layers in thickness	2	4	2	–
Fibre architecture	Random fibre veil	+45°/90°/–45°/CSM	156 (56 yield)	–
% volume fraction	3	34	33	30
% total of fibre reinforcement	5	48	47	–
Nominal layer thickness, t_{lay} (mm)	0.03	1.4	2.0	–

Table 2. Lamina properties for the laminate defined in Fig. 2.

Elastic lamina properties (kN/mm^2)	Constituent part: UD	Constituent part: TSFM – Mat layer (+45°/90°/–45°)	Constituent part: TSFM – CSM	Laminate strength properties (N/mm^2)		Fracture energy (N/mm)	
E_1	44.7	13.1	7.7	$f_{1,T}$	294	$G_{1,T,c}$	100
$E_2 = E_3$	14.0	25.5	7.7	$f_{1,C}$	306	$G_{1,C,c}$	100
$G_{12} = G_{13}$	4.1	6.1	2.7	$f_{2,T}$	84	$G_{2,T,c}$	1.2
ν_{12}	0.28	0.41	0.41	$f_{2,C}$	133	$G_{2,C,c}$	5
				$f_{1,S} = f_{2,S}$	91		

Table 3. Interfacial properties for the pultruded FRP laminate defined in Fig. 2.

Interfacial properties	
$K_{I} = K_{II} = K_{III}$ (N/mm^3)	10^6
f_{I} (N/mm^2)	21[1]
$f_{II} = f_{III}$ (N/mm^2)	23[1]
$G_{I,c}$ (N/mm)	0.2
$G_{II,c} = G_{III,c}$ (N/mm)	0.5

Note. These values correspond to a weakening factor of 0.25.

Table 4. Modelling results: relative thickness of layers.

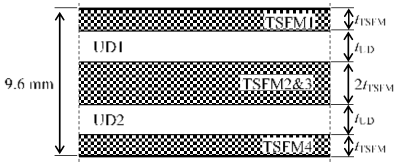		**M12**					**M20**				
		S_{el} (kN/mm)	$R_{br,ID}$ (kN)	$R_{br,max}$ (kN)	$R_{br,ID}/R_{br,max}$	$R_{br,max}/R_{br,max,baseline}$	Sel (kN/mm)	$R_{br,ID}$ (kN)	$R_{br,max}$ (kN)	$R_{br,ID}/R_{br,max}$	$R_{br,max}/R_{br,max,baseline}$
Original material											
t_{TSFM} (mm) (% of t) t_{UD} (mm) (% of t)	1.4 (58) 2.0 (42)	59	17	23	0.75	1.00	82	27	36	0.75	1.00
Parametric variation											
t_{TSFM} (mm) (% of t) t_{UD} (mm) (% of t)	1.0 (42) 2.8 (58)	69	19	23	0.82	1.02	95	31	35	0.89	1.00
t_{TSFM} (mm) (% of t) t_{UD} (mm) (% of t)	1.2 (50) 2.4 (50)	65	15	23	0.63	1.01	74	25	35	0.73	1.00
t_{TSFM} (mm) (% of t) t_{UD} (mm) (% of t)	1.6 (67) 1.6 (33)	58	20	24	0.87	1.05	88	28	35	0.81	1.01

Table 5. Modelling results: thickness of internal TSFM layer.

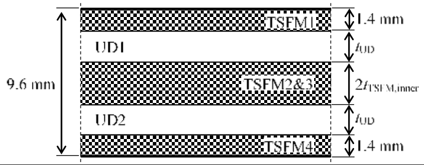		M12					M20				
		S_{el} (kN/mm)	$R_{br,ID}$ (kN)	$R_{br,max}$ (kN)	$R_{br,ID}/R_{br,max}$	$R_{br,max}/R_{br,max,baseline}$	S_{el} (kN/mm)	$R_{br,ID}$ (kN)	$R_{br,max}$ (kN)	$R_{br,ID}/R_{br,max}$	$R_{br,max}/R_{br,max,baseline}$
Original material											
$t_{TSFM,inner}$ (mm) t_{UD} (mm)	($1.0t_{orig}$) 1.4 2.0	59	17	23	0.75	1.00	82	27	36	0.75	1.00
Parametric variation											
$t_{TSFM,inner}$ (mm) t_{UD} (mm)	($0.5t_{orig}$) 0.7 2.7	72	19	23	0.83	0.99	94	30	37	0.82	1.02
$t_{TSFM,inner}$ (mm) t_{UD} (mm)	($0.25t_{orig}$) 0.35 3.05	77	20	25	0.80	1.11	102	31	37	0.83	1.03
$t_{TSFM,inner}$ (mm) t_{UD} (mm)	($0.15t_{orig}$) 0.21 3.19	80	17	25	0.68	1.10	99	33	36	0.92	1.01
$t_{TSFM,inner}$ (mm) t_{UD} (mm)	($0t_{orig}$) 0 3.4	75	21	25	0.83	1.08	105	32	38	0.84	1.06

Table 6. Modelling results: stacking sequence TSFM layer.

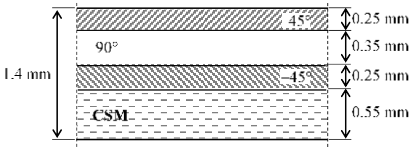

		M12					M20				
		S_{el} (kN/mm)	$R_{br,ID}$ (kN)	$R_{br,max}$ (kN)	$R_{br,ID}/R_{br,max}$	$R_{br,max}/R_{br,max,baseline}$	S_{el} (kN/mm)	$R_{br,ID}$ (kN)	$R_{br,max}$ (kN)	$R_{br,ID}/R_{br,max}$	$R_{br,max}/R_{br,max,baseline}$
Original material											
$t_{TSFM,1}$ $t_{TSFM,2}$	+45°/90°/-45°/CSM +45°/90°/-45°/CSM	59	17	23	0.75	1.00	82	27	36	0.75	1.00
Variation											
$t_{TSFM,1}$ $t_{TSFM,2}$	+45°/90°/-45°/CSM CSM /-45°/90°/45°	59	19	24	0.77	1.05	82	27	35	0.79	0.96
$t_{TSFM,1}$ $t_{TSFM,2}$	CSM /-45°/90°/45° +45°/90°/-45°/CSM	59	20	23	0.87	1.01	82	33	37	0.88	1.08
$t_{TSFM,1}$ $t_{TSFM,2}$	CSM /-45°/90°/45° CSM /-45°/90°/45°	59	20	23	0.88	1.01	82	33	40	0.82	1.16